Fracture pinning and b-value of micro-seismicity

Jean Schmittbuhl,[1] Arne Stormo,[1] Olivier Lengliné,[1] Camille Jestin,[1] and Alex Hansen[2]

[1]*IPGS, EOST, CNRS, Université de Strasbourg, 5 rue René Descartes, 67084, Strasbourg, France*

[2]*Department of Physics, Norwegian University of Science and Technology, N-7491, Trondheim, Norway*

(Dated: October 4, 2015)

I. INTRODUCTION

The distribution of induced-earthquake magnitudes in deep geothermal reservoirs is a classical tool for monitoring reservoirs. It typically shows some important fluctuations through time and space. Despite being a very crude information (i.e. a scalar quantity) of very complex mechanical stress evolution, understanding these variations could still give us insights into the mechanics of the reservoir. Here we analyse the output of a simple quasi-static physical model of a single fault with the support of experimental results and propose a new way to describe bursts that could be compared to seismic events [1].

Crack propagation in heterogeneous media is a rich problem which involves the interplay of various physical processes. The problem has been intensively investigated theoretically, numerically, and experimentally, but a unifying model capturing all the experimental features has not been entirely achieved (see [2] for a recent review) despite its broad range of implications in engineering and Earth sciences problems [e.g. 3, 4]. The slow propagation of a crack front where long range elastic interactions are dominant, is of crucial importance to fill the gap between experiments and models. Several theoretical and numerical works have been devoted to quasi-static models. Such models give rise to an intermittent local activity characterized by a depinning transition and can be viewed as a critical phenomenon [2]. However these models fail to reproduce all experimental conditions, notably the front morphology does not display any cross-over length with two different roughness exponents above and below the cross-over as observed experimentally [e.g. 5].

During most regular fracture experiments, the fracture surface can only be observed post mortem. In an attempt to study the dynamical properties of the fracture, Schmittbuhl and Måløy [6] developed an experiment where they forced the fracture to develop in a weak plane of a transparent medium (PMMA). In such an experimental configuration, the propagation of the fracture front can the be explored using high resolution optical devices from which different properties characterizing the fracture dynamics can be inferred. Distribution of the local fracture velocities [7] or morphology of the fracture front [5] can notably be measured and are found to be robust parameters when tested against several experimental conditions.

Since Mandelbrot's discovery [8] that fracture surfaces in metal display fractal properties, there have been many attempts to understand the scaling relations of fracture. In particular, the self-affine nature of fracture surfaces have come under much scrutiny. A self-affine surface $h(x)$ has the following scaling relation [9]

$$h(x) \propto \lambda^{\zeta} h(\lambda x). \tag{1}$$

λ is an arbitrary scaling factor, and ζ is the roughness exponent. The scaling relations for fractures have now been established as scale and direction dependant (Ponson et al. [10, 11], Bonamy et al. [12]). In 2010 Santucci et al. [5] found that the in-plane fractures also had a scale dependant roughness exponent. At small scales they obtained $\zeta^- = 0.60$, while at large scales they showed that $\zeta^+ = 0.35$. Attempts to model the behaviour of the in-plane fracture process had a long time resulted in only the large scale roughness exponent (Schmittbuhl et al. [13], Rosso and Krauth [14]), or the small scale roughness exponent in the context of a stress-weighted percolation (Schmittbuhl et al. [15]).

More recently, Gjerden et al. [16] presented for the first time roughness exponents compatible with both the large scale and small scale values found in the experiments. Their model was a development of the elastic fiber bundle model presented by Batrouni et al. [17]. In this model, the fracture front is the result of an artificially directional preference for the damage development owing to a linear gradient in the fiber strength.

We compare here experimental observations of a slow interfacial crack propagation along an heterogeneous interface to numerical simulations using a cantilever fiber bundle model. The model consists of a planar set of brittle fibers between an elastic half-space and a rigid plate with a non linear shape which loads the system in a cantilever configuration. The non linear square root shape combined to long range interactions is shown to provide an more realistic displacement and stress field in the process zone around the crack tip and significantly improved the prediction of the model. Experiments and models are shown to share a similar self-affine roughening of the crack front both at small and large scales, a similar Family-Viscek transient scaling and a similar distribution of the local crack front velocity.

II. EXPERIMENTAL SETUP

The experimental setup used in the interfacial crack experiments we will compare our numerical simulations with, consists of two transparent welded PMMA (poly methyl methacrylate) plates [e.g. 6, 7, 18, 19]. Disorder

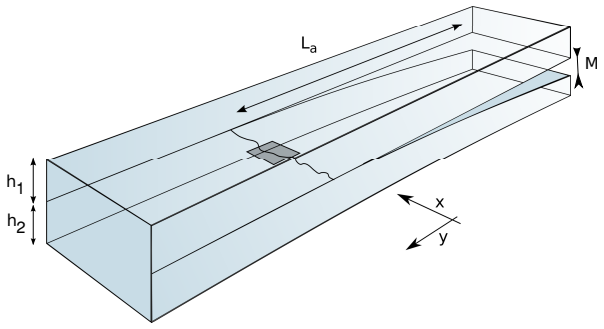

FIG. 1: Sketch of the experimental setup. Two PMMA plates of thickness h_1 and h_2 are welded and a mode I fracture propagates at the interface between the two plates. Fracture propagation is caused by the opening, M, between the two plates. The distance between the loading point and the crack front is noted L_a. The crack front propagates along the y direction. The gray rectangle marks the area around the crack front we will reproduce in our simulations.

is first introduced on the surfaces of the plates by sandblasting glass beads of variable diameters (180-300μm). Welding of the two plates is then achieved by imposing a normal load on the assembled plates while heating the system at 190^{o}C. This thermal annealing produces a cohesive interface weaker than the bulk, along which the sample will break under normal loading.

The upper plate is finally attached to a stiff aluminum frame while a load is applied over the top side of the bottom plate in a direction normal to the plate interface. The vertical displacement imposed on the bottom plate induces stable mode I propagation of a planar fracture along the prescribed weak interface. A sketch of the experiment is given in Figure 1. The fracture front creates an optical contrast between the broken and unbroken part. This fracture front is then tracked by an optical camera in order to extract its position through time.

The front propagates along the y axis where the origin is defined at the loading point and is positive in the direction of crack propagation. The x axis is perpendicular to y and defines the coordinate of a point along the front. Sample dimensions are variable but are typically 20 cm long, 3 cm wide and 5 mm thick for the bottom plate and 1cm thick for the upper plate. The large scale bending of the plate at the sample size is well reproduced by the elastic beam theory [19]. At a smaller scale i.e. at the scale of the process zone, the elastic beam theory might however not be any more valid in describing the shape of the plate and typical crack solutions eventually provide more a realistic description.

III. MODEL

The soft-clamped fiber bundle model was first introduced by Batrouni et al. [17] in 2002. We use this model

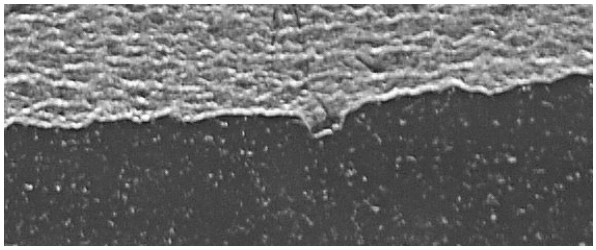

FIG. 2: Picture of the crack front area obtained during an experiment. The crack is propagating from top to bottom, the gray part refers to already broken part and the dark area to the unbroken part. The optical contrast between this two parts defines the fracture front. The dimension of the picture in the x-direction is 4 mm.

in order to reproduce the phenomena occurring at the process zone scale around the fracture front. We are indeed interested in parameters controlling the behaviour of the fracture front at a short range from its edge. We thus consider our model as a square of dimension $L_f \times L_f$ around the fracture front. This area of the system is illustrated in Figure 1 by the dark square covering a part of the fracture front. This area is divided into $N \times N$ sub-squares, each of them containing a single fiber. A discretization size is then $dl = L_f/N$. The two facing Plexiglas plates are represented as infinite facing half-spaces, and act as clamps attached to the N^2 fibers. The half-spaces are supposed to have an elastic behavior with a Youngs modulus E and a Poisson ratio of ν. An equivalent simpler configuration can be obtained by assuming that one of the half-spaces is infinitely stiff. Thus E will only describe the elastic response of the other half-space. The system is supposed to be periodic in all directions. For a full description of the numerical implementation we refer to Batrouni et al. [17].

The fibers are linearly elastic up to a strength threshold where they break irreversibly and can no longer support any load. The thresholds are uniformly distributed between $f^t_{\min}$ and $f^t_{\max}$. The force, f_i, experienced by each individual fiber is given by the Hooke's law:

$$f_i = -k(u_i - D_i), \tag{2}$$

where i is the index of the fiber, k is the spring constant, equal for all the fibers, D_i is the locally imposed displacement between the clamps and u is the local deformation of the clamps due to the force landscape created by the surounding fibers. This spatially dependant deformation is calculated by Love's law [20]:

$$u_i = \sum_{j \neq i}^{N^2} G_j f_j \tag{3}$$

where j runs over all the fibers in the array (except the self-induced contribution). The Green's function G_j is

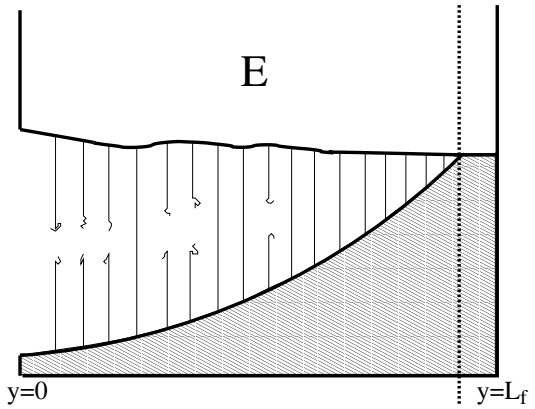

FIG. 3: Sketch of the loading of the fiber-bundle model. Individual fibers are represented by dark vertical lines and can be broken or unbroken. The shape of the bottom plate follows the displacement $D \propto \sqrt{L_f - y}$, as given by equation (5) [22]

given by:

$$G_j = \frac{1-\nu^2}{\pi E dl^2} \int_{-dl/2}^{+dl/2} \int_{-dl/2}^{+dl/2} \frac{dx'\ dy'}{|\vec{r}_i(0,0) - \vec{r}_j(x',y')|}, \quad (4)$$

The integrals in Eq.(4) runs over the dl^2 square associated with the fiber j. The x' and y' coordinates have their origin in the middle of the discretization areas where the fibers are attached. The vector r represents the distance from the origin of the system to (x', y') for each fiber.

The large scale displacement of the bottom plate recorded in experiments is well reproduced by an elastic beam model [21]. At the process zone scale however, the crack tip opening is strongly influences by the crack geometry. At the scale of our investigation, *i.e.* close to the fracture front, we adopt an elastic crack solution. Indeed, the crack tip opening $\delta(y) = D(y) - u(y)$ is then proportional to the square root of the distance $y_c - y$ to the fracture front [22]:

$$\delta(y_c - y) = \frac{8(1-\nu^2)}{\sqrt{2\pi}} \left(\frac{K}{E}\right) \sqrt{y_c - y} \quad (5)$$

where y_c is the position of the crack tip and K is the stress intensity factor. We test this solution by imposing a flat shape $D(y) = D_0$ of the rigid plate and assuming that half of the fibers are broken.

In order to mimic the displacement behaviour of equation (5) over a larger scale behind the crack tip, we chose to impose the following shape:

$$D(y) = D_0 \sqrt{L_f - y}, \quad (6)$$

to the rigid plate where D_0 is an arbitrary scaling prefactor. This loading scheme is illustrated in Figure 3.

The system is updated iteratively and quasistaticaly by removing the fibers one by one. At each step we compute a new prefactor D_0 in equation 6 that will correspond to a force field where only one of the fibers is experiencing a force equal to its strength threshold. This fiber is actually the closest one to failure and thus requires the least increase of D_0 to break. This fiber is then removed and the procedure is continued until there is no intact fiber left.

A. Length scales in the model

When the distances are measured in units of the discretization size dl, the relative influence of the elastic interactions with respect to the global loading have been found to be described by a single parameter named the reduced Young's modulus [23]

$$e = \frac{Edl}{N}. \quad (7)$$

where E is the Young's modulus, N the number of fibers per system length L_f. Indeed, the contribution of the Green function in the force computation of each fiber can be turned on or off, depending on the value e. In the stiff regime, i.e. large e, the fracture process is dominated by a diffusive damage controlled by the strength heterogeneities in the system. When e decreases, the system goes trough a cross-over regime where the influence of the elastic forces rises. When e is sufficiently low, the competition between the elastic redistribution and the strength heterogeneities are balanced and the system enters a so-called soft regime. This regime is dominated by localized damage. As we can see from equation (7), decreasing E, while increasing N in a way that keeps e constant is not affecting the influence of the Green function. We will thus associate the soft systems with large length scales. Similarly, we will associate the stiff systems with short length scales.

IV. RESULTS

A. Front morphology: self-affine caling and cross-over length scale

Previous experimental studies reported that an interfacial crack front in the present configuration is self-affine with a roughness exponent $\zeta \simeq 0.6$ [e.g. 6, 18]. More recent data extracted from numerous experiments and at various scales show that actually two distinct regimes emerge depending on the scale of investigation: at small scales the scaling regime is characterized by a roughness exponent $\zeta^- \simeq 0.60$ while at large scale the exponent is lower and is found around $\zeta^+ \simeq 0.35$ [5]. We aim at comparing the scaling properties of the simulated crack front to experimental observations. For this, we identify the fracture front as the interface between the cluster of broken fibers spacially connected (*i.e.* in the sense of a link between first neighbors) to one side of the system and the cluster of surviving fibers connected to the other side. When this interface is identified, it is approximated

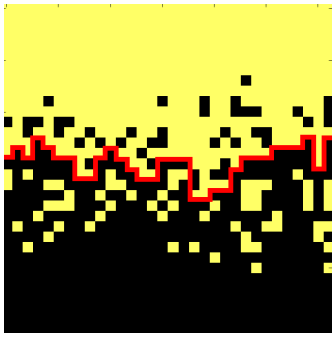

FIG. 4: Example of a fracture front trace during a simulation for a stiff system. The dark points refer to broken fibers while yellow points are intact fibers. The system size is N=32. The red line represents the fracture front following a SOS algorithm (see text).

FIG. 5: Same as figure 4 for a soft system.

as a function of the x-coordinate for each time step t: $h(x,t)$ by using a solid-on-solid (SOS) algorithm. The front line is indeed deduced by taking the first y-value hit when searching along the y-axis from above or below. An example of this front is given by the red line in Figure 4 for stiff systems, and in Figure 5 for soft systems.

We investigated the scaling properties of the crack front morphology in our simulations. In order to find the roughness exponent (cf Eq. 1) of the fracture fronts produced by our model, we analyzed them using the average wavelet coefficient method [24]. This gives us a roughness exponent of $\zeta_- = 0.53 \pm 0.02$ for stiff systems. We also realized simulations in the soft regime, i.e., representing large length scales. Similarly, we extracted front positions and computed the wavelets coefficients from the front morphology. We obtained the roughness exponent by fitting the four largest coefficients for $L = 128$. This gives: $\zeta_+ = 0.35 \pm 0.01$. As opposed to the short scale regime, the estimated value of ζ_+ is nearly insensitive to the system size. We also observe that the experimental roughness exponent observed at large length scale [5] is similar to the one we obtained from our simulations.

B. Distribution of local velocity and velocity burst distribution

A direct way for studying the dynamics of the fracture propagation is to measure the distribution of the local velocity along the crack front. To obtain this we use the waiting time matrix technique developed by Måløy et al. [7] on experimental data. Comparisons with experimental data show a good agreement. We notably recover in the simulation a similar heterogeneous pattern of the local crack speed.

Experimentally the distribution of the local velocities v have been found to follow the relation:

$$P(v/\langle v\rangle) \propto (v/\langle v\rangle)^{-\eta}, \quad \text{for}(v/\langle v\rangle) > 1, \tag{8}$$

where $\eta = 2.55 \pm 0.15$ and is found to be a robust feature over many experiments [7, 25, 26]. In a previous fiber bundle model Gjerden et al. [27], following the same procedure for computing the waiting time matrix, found that, at large scale i.e. for soft systems, the velocity distribution is well fitted by an equation of the form of Eq. (8) with an exponent $\eta = 2.53$ close to the experimental value. We see that the two regimes produce a power-law decay of the velocity distribution above the average crack velocity. The best power law fits for the two regimes, stiff and soft regimes, give $\eta_- = 2.89$ and $\eta_+ = 2.54$ respectively. Such values are very close to the experimental exponent $\eta = 2.55$, especially for the soft system.

Damage burst distribution, b_b

In order to compare our model to the one presented by Amitrano [28], we want to find the distribution of temporal damage bursts. We can then extract a burst distribution exponent b_b-value from our system using the event-size distribution. We recall that we define the size of an event δ, as the number of fibers that are broken for each increase of the load Σ. We run the elastic fiber-bundle model for both the stiff ($e = 32$) regime with diffuse ductile failure, and the soft ($e = 7.63 \cdot 10^{-6}$) regime with localized brittle failure. This is done for both regimes at $L = [32, 64, 128, 256]$. The slope of 1.475 for the linear trend for $\delta/L^\gamma \leq 1$ is consistent with the theoretical 1.5 burst exponent for the equal load sharing fiber bundle model (see Pradhan et al. [29], Hemmer and Hansen [30] and Pradhan et al. [31]). This gives us a size independent stiff b_b-value of 1.475 for $L = [32, 64, 128, 256]$.

V. CONCLUSIONS

Our model is an elastic fiber bundle model describing multiple ruptures along a single major fault of the reservoir. It consists of a set of fibers with various strengths, arranged in a planar $L \times L$ two dimensional array, linking

together two elastic half-spaces. It mimics a fault zone with various asperities. During load, the fibers break quasi-statically according to a stress threshold distribution. On the contrary to classical fiber bundle model, here when a fiber breaks, it redistributes the load on the surviving fibers through long range elastic interactions. Interestingly, the elasticity of the half-spaces which changes the range of the stress distribution, characterizes two distinct regimes. In a stiff regime we find an effective ductile deformation regime at large scale since the damage distribution is very difuse. Conversely in softer systems, the distance between two consecutive breaking fibers gets smaller and failure of the interface is localized, exhibiting an effective brittle regime. We analyse two types of burst distributions: a classical one built from the statistics of the broken bonds during each failure step and a new one defines from a waiting time matrix of the fracture front propagation. The first one reproduces several known results for this type of model. The new one evidences the existence of effective creeping advances of the front with statistics that follow a Gutenberg-Richter distribution in particular in the ductile regime (stiff systems). We proposed a new definition of bursts in a fault model, based on the local fracture front velocity. We find that b_v-values for the distribution of the velocity clusters are very consistent with Gutenberg-distribution of induced seismicity. We link the b_v-value fluctuations in the reservoirs to the influence of the velocity threshold level that could be related to recording limitation. b_b-values obtained from the broken bond statistics are hardly comparable to seismic events because of the lack of space contiguousness of broken fibers during bursts. In the light of our results, we discuss the implications of b-value changes in geothermal reservoir in terms of fault asperities and normal stress evolution.

Acknowledgments

We thank K. S. Gjerden, K. J. Maloy for insightful discussions and acknowledge the support of ANR SUPNAF and Labex G-eau-thermie Profonde .

[1] A. Stormo, O. Lengliné, and J. Schmittbuhl, Geothermal Energy **3**, 1 (2015).
[2] D. Bonamy and E. Bouchaud, Physics Reports **498**, 1 (2011), ISSN 0370-1573.
[3] T. L. Anderson, *Fracture mechanics: fundamentals and applications* (CRC press, 2005).
[4] C. H. Scholz, *The Mechanics of Earthquakes and Faulting* (Cambridge University Press, 2002).
[5] S. Santucci, M. Grob, R. Toussaint, J. Schmittbuhl, A. Hansen, and K. Maløy, EPL (Europhysics Letters) **92**, 44001 (2010).
[6] J. Schmittbuhl and K. J. Måløy, Physical review letters **78**, 3888 (1997).
[7] K. J. Måløy, S. Santucci, J. Schmittbuhl, and R. Toussaint, Physical review letters **96**, 045501 (2006).
[8] B. B. Mandelbrot, D. E. Passoja, and A. J. Paullay (1984).
[9] A.-L. Barabási, *Fractal concepts in surface growth* (Cambridge university press, 1995).
[10] L. Ponson, D. Bonamy, and E. Bouchaud, Physical review letters **96**, 035506 (2006).
[11] L. Ponson, H. Auradou, P. Vié, and J.-P. Hulin, Physical review letters **97**, 125501 (2006).
[12] D. Bonamy, L. Ponson, S. Prades, E. Bouchaud, and C. Guillot, Physical review letters **97**, 135504 (2006).
[13] J. Schmittbuhl, S. Roux, J.-P. Vilotte, and K. J. Måløy, Physical review letters **74**, 1787 (1995).
[14] A. Rosso and W. Krauth, Physical Review E **65**, 025101 (2002).
[15] J. Schmittbuhl, A. Hansen, and G. G. Batrouni, Physical review letters **90**, 045505 (2003).
[16] K. S. Gjerden, A. Stormo, and A. Hansen, Physical review letters **111**, 135502 (2013).
[17] G. G. Batrouni, A. Hansen, and J. Schmittbuhl, Physical Review E **65**, 036126 (2002).
[18] A. Delaplace, J. Schmittbuhl, and K. J. Måløy, Physical Review E **60**, 1337 (1999).
[19] O. Lengliné, R. Toussaint, J. Schmittbuhl, J. E. Elkhoury, J. Ampuero, K. T. Tallakstad, S. Santucci, and K. J. Måløy, Physical Review E **84**, 036104 (2011).
[20] A. E. H. Love, Philosophical Transactions of the Royal Society of London. Series A, Containing Papers of a Mathematical or Physical Character pp. 377–420 (1929).
[21] O. Lengliné, J. Schmittbuhl, J. Elkhoury, J.-P. Ampuero, R. Toussaint, and K. J. Måløy, J. Geophys. Res. **116** (2011).
[22] J. Rice, Journal of Applied Mechanics **52**, 571 (1985).
[23] A. Stormo, K. S. Gjerden, and A. Hansen, Physical Review E **86**, 025101 (2012).
[24] I. Simonsen, A. Hansen, and O. M. Nes, Physical Review E **58**, 2779 (1998).
[25] K. T. Tallakstad, R. Toussaint, S. Santucci, J. Schmittbuhl, and K. J. Måløy, Physical Review E **83**, 046108 (2011).
[26] O. Lengliné, J. Elkhoury, G. Daniel, J. Schmittbuhl, R. Toussaint, J.-P. Ampuero, and M. Bouchon, Earth Planet. Sci. Lett. **331-332**, 215 (2012).
[27] K. S. Gjerden, A. Stormo, and A. Hansen, arXiv:1308.5800 (2013).
[28] D. Amitrano, Journal of Geophysical Research: Solid Earth (1978–2012) **108**, 2044 (2003).
[29] S. Pradhan, A. Hansen, and B. K. Chakrabarti, Reviews of modern physics **82**, 499 (2010).
[30] P. C. Hemmer and A. Hansen, Journal of applied mechanics **59**, 909 (1992).
[31] S. Pradhan, A. Hansen, and P. C. Hemmer, Physical review letters **95**, 125501 (2005).